ECS Transactions, 61 (1) 109-120 (2014)
10.1149/06101.0109ecst ©The Electrochemical Society

Three Dimensional Microstructural Characterization of Cathode Degradation in SOFCs Using Focused Ion Beam and SEM

J. A. Taillon, C. Pellegrinelli, Y. Huang, E. D. Wachsman, and L. G. Salamanca-Riba

Department of Materials Science and Engineering, University of Maryland, College Park, Maryland 20742, USA

Composite cathodes in solid oxide fuel cells (SOFCs) improve performance by increasing the triple phase boundary length and providing a more continuous pathway through the electrolyte for oxygen ion transport. These cathodes however, are susceptible to performance degradation from exposure to contaminants such as H_2O and CO_2 vapor. The microstructure and connectivity of yttria-stabilized zirconia (YSZ)/lanthanum strontium manganite (LSM) composite cathodes were examined and quantified using a dual beam focused ion beam/scanning electron microscope (FIB/SEM) in order to determine the effect of various contaminants on the performance of the SOFCs. Three-dimensional reconstructions of multiple composite cathodes allowed for microstructure quantification at nanometer resolution. Further analysis of triple phase boundary length (L_{TPB}) demonstrated how the available active sites changed as a function of cell operation and contamination. This sort of analysis allows for a direct comparison between cathode microstructure and polarization resistance.

Introduction

Solid oxide fuel cells (SOFCs) are very promising, fuel flexible electrochemical devices that can be used to generate heat and electrical power. Their limited durability in practical applications, however, has impeded wide scale commercial adoption of the technology. One of the leading causes of performance loss is due to degradation in the cathode layer with long-term exposure to various contaminants such as H_2O and CO_2 vapor (1). This degradation leads to significant compositional and microstructural changes that adversely affect activation, polarization mechanisms, and ionic and electronic conductivities. Previous works have demonstrated that quantifiable microstructural characteristics can be directly related to SOFC performance, the most important of these being active triple phase boundary length (L_{TPB}) and pore surface area (2, 3).

In this work, the microstructure of two composite cathode structures was analyzed and quantified using a dual beam focused ion beam/scanning electron microscope (FIB/SEM) nanotomography technique to serially mill and image slices of a sample volume. These images were then used to calculate a direct three-dimensional reconstruction of the active region at nanometer scale. Improvements have been made to sample preparation and data acquisition procedures, as well as post-acquisition data processing, and are described. Initial results between two samples are presented and discussed: an unaged baseline sample (with no exposure to contaminants), and one aged under H_2O ambient. In coming works, the performance of these degraded cells will be correlated with the measured changes in their microstructure, developing quantitative models for the effects of cathode degradation on microstructure.

Experimental Details

Button Cell Fabrication and Exposure

Symmetric cathode cells were produced by standard screen printing methods using a dense sintered yttria-stabilized zirconia [$(Y_2O_3)_{0.08}$-$(ZrO_2)_{0.92}$, YSZ] electrolyte (Tosoh USA, Inc.), and a composite cathode. The composite cathode source paste consisted of 50% lanthanum strontium manganite [$(La_{0.8}Sr_{0.2})_{0.95}MnO_{3-x}$, LSM] and 50% 8-YSZ by weight (Fuel Cell Materials). Cells were fabricated by screen printing two layers of composite cathode paste and sintering at 1000ºC for 1hr, resulting in cathode layers approximately 35µm thick on a bulk (500 µm thick) electrolyte (see Figure 1). We report here the quantification of and differences between two LSM-YSZ/YSZ/LSM-YSZ symmetric cells: as fabricated (referred to henceforth as *unaged*), and aged under H_2O atmosphere (referred to as *H_2O*). The H_2O-exposed sample was aged at 800ºC for approximately 500 hours under a 3% H_2O atmosphere (flow rate of 100 sccm), introduced by flowing room temperature synthetic air through room temperature water.

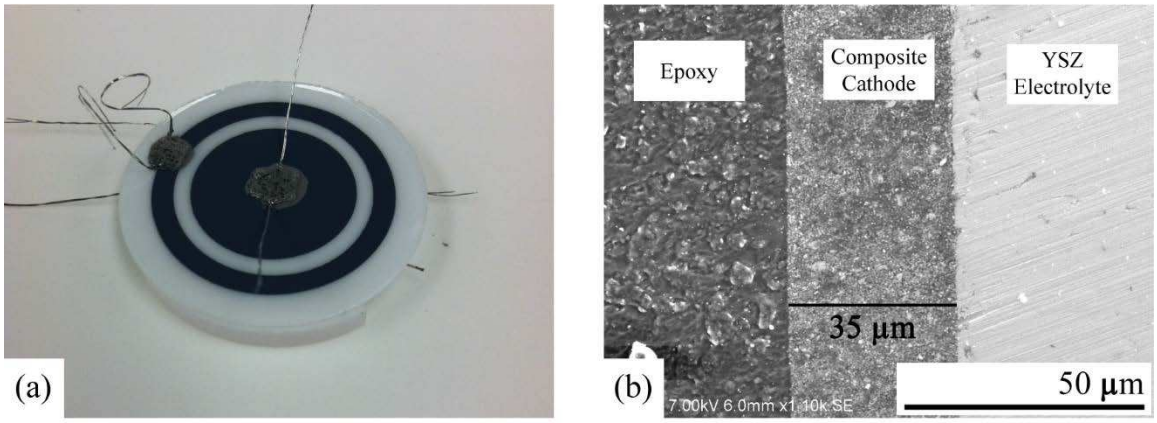

Figure 1. (a) Image of symmetric cathode button cell after fabrication and preparation for electrical impedance testing. (b) Cross sectional scanning electron micrograph of epoxy-impregnated cell, showing overall structure of cathode.

FIB/SEM Sample Preparation

A number of preparatory steps were necessary to ensure electron images that were free of artifacts and with sufficient contrast to discern the two components of the composite cathode:

In order to prevent “curtaining” from appearing in the images due to inhomogeneous milling (a common FIB artifact), the porous cathode structure was impregnated with an epoxy resin. The epoxy impregnation procedure also enhances image contrast and ensures that only material on the current slice appears in each image, since the low-voltage (2 kV) SEM will not penetrate deep into the epoxy. A VacuPrep (Allied High Tech) system was used to impregnate the porous cathode under vacuum with a low viscosity epoxy resin (EpoxySet, Allied High Tech). Using the neat resin, significant charging was encountered during FIB/SEM observation. To alleviate this, the epoxy resin was loaded with 1.2 vol. % acetylene black (MTI Corporation), dispersed using 10 minutes of probe sonication. This process enhanced the conductivity of the epoxy matrix, and when combined with low-voltage imaging parameters, allowed for high resolution and artifact free images.

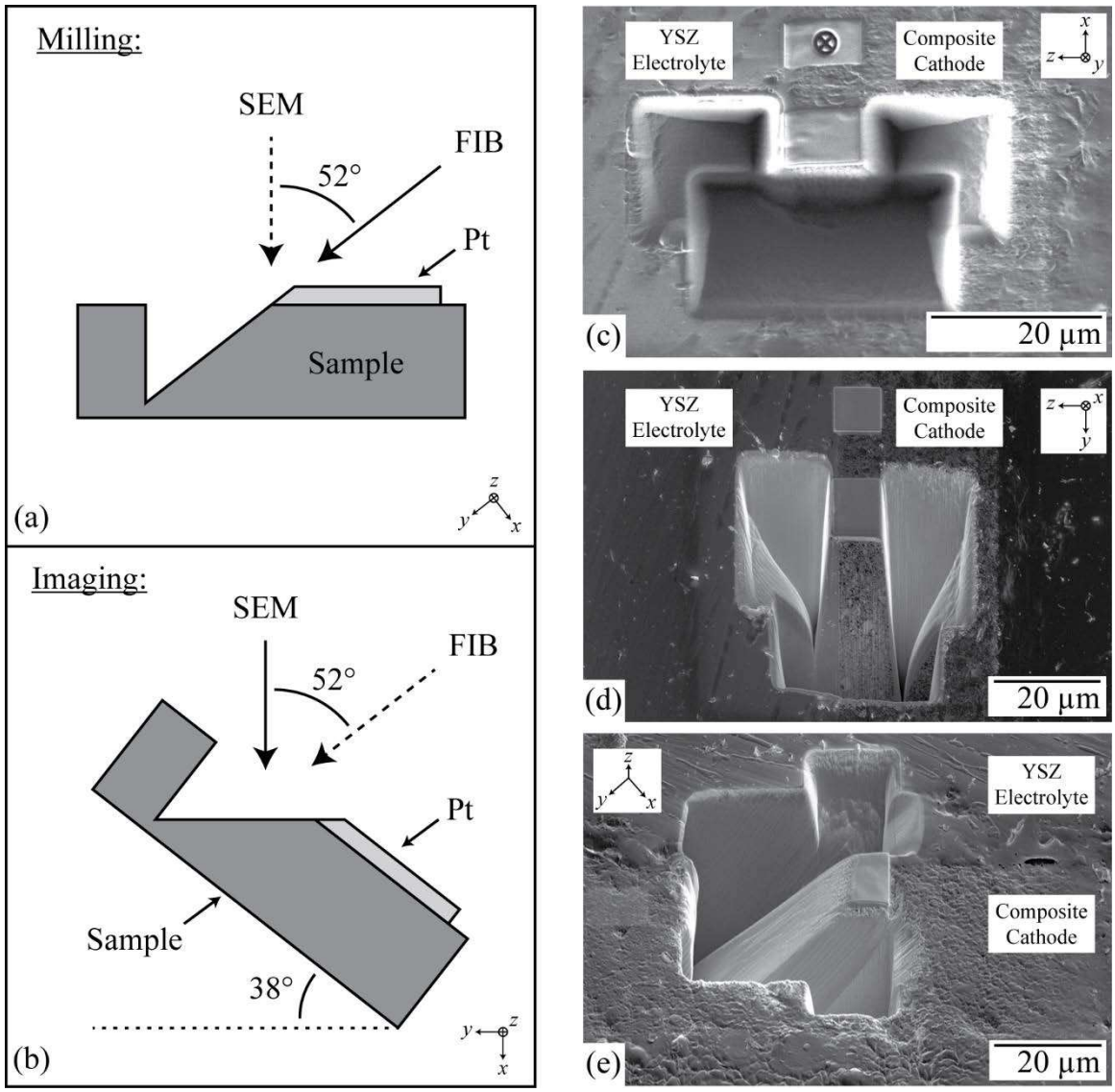

Figure 2. Side-view schematics of the orientations used during the (a) milling and (b) imaging steps for each slice. The SEM and FIB columns are at a fixed offset of 52º. When milling at 0º, images can be taken perpendicular to the sample surface by tilting the stage by 38º (as shown in (b)). (c) FIB image taken from the milling position, showing both the ion beam fiducial mark and the "C trench" that was milled to prevent redeposition. The area of interest is covered by a protective Pt pad. (d) SEM image taken from the imaging position showing the same features. The face of the porous composite cathode is visible in this image, as well as the protective Pt and the Pt for the ion beam fiducial (image taken before milling the fiducial). (e) Side-view SEM image of the area of interest (image taken prior to cleaning redeposition from the sample face). The stage was rotated by 90º and tilted to 52º to roughly match the orientation shown in (a). The *x*, *y*, and *z* directions (as referenced in the text) are defined in each image.

Once mounted in epoxy, the sample was mechanically planarized with SiC abrasives ranging from 400 – 1200 grit and polished with a 3 µm diamond suspension using a MetPrep-3 (Allied High Tech).

Due to the poor contrast between YSZ and LSM with traditional imaging settings, it was necessary to modify the sample geometry and imaging conditions from those used in prior works (4, 5) in order to generate sufficient contrast between the two phases. Primary among these was a change to the milling orientations that allows for improved SEM imaging perpendicular to the sample face when using the through lens electron detector (TLD). This alignment increases the fraction of secondary electrons that are ejected

towards the detector, improving detector gain and the resulting image contrast. The modified orientation also limits the shadowing that occurs towards the bottom of each image when imaged at an acute (52°) angle. This improvement comes at the expense of additional time required to orient the stage before milling each slice. The primary preparation steps involve depositing a protective Pt layer over the region of interest (ROI), milling a distinct ion beam fiducial mark, milling a "C-trench" around the ROI, and polishing the sample face using a cleaning cross-section pattern. Figure 2 shows schematics of the sample orientation for each step, as well as overview FIB/SEM images of the sample area during FIB preparation.

FIB/SEM Slice and View

Once the samples were fully prepared, an FEI Helios NanoLab 650 FIB/SEM was combined with the Auto Slice and View G3 software (FEI) to automatically mill and image serial slices (in the *x* direction) through the ROI, yielding a stack of 2D images. The slice thickness used in this work was 30 nm, which was sufficiently small to accurately reconstruct the smallest particles encountered (6). Typically, at least 150 slices were obtained during each experiment. The imaging orientation used in this work also differed from previous studies on SOFC cathodes (4, 5). Rather than milling slices parallel to the cathode/electrolyte interface, this work used slices milled orthogonal to this direction, ensuring that the interface was present in every image, thus improving the reliability of the reconstruction near the phase boundary.

Optimization of imaging parameters was required in order to obtain the best contrast between each phase in the composite cathode. The SEM was operated at a 2 kV accelerating voltage and 100 pA beam current, with a 3 μs dwell time per pixel at a 4 mm working distance. The gain of the TLD was maximized and the suction voltage increased to the maximum 245 V to attract the greatest number of electrons. During the course of imaging, it was observed that the contrast of each phase improved after initial exposure to the electron beam, due to a small degree of charging in the YSZ regions, causing them to become significantly brighter after exposure. To exploit this, the auto-focus routine present in the Slice and View software was used to ensure each slice was pre-exposed before final imaging. Example SEM images are displayed in Figure 3(a). The dimensions shown in these images are typical, and result in reconstructed volumes of approximately 300 - 400 μm^3. This is on the same order as volumes used in previous works (5, 7), and contains enough discrete particles to be considered a representative volume.

Post-acquisition Data Analysis

Once the images were acquired, subsequent data analysis was performed using the Avizo Fire software package (FEI Visualization Sciences Group).

Image Post-processing. After acquisition, each image was filtered using a two-dimensional non-local means filter. The algorithm used is particularly effective at denoising FIB/SEM images and operates by comparing the neighborhoods of each voxel in the image (8). Once denoised, the image stack was cropped to the area of interest, and aligned using either the automated least-squares alignment procedure in Avizo, or the StackReg plugin for Fiji (9).

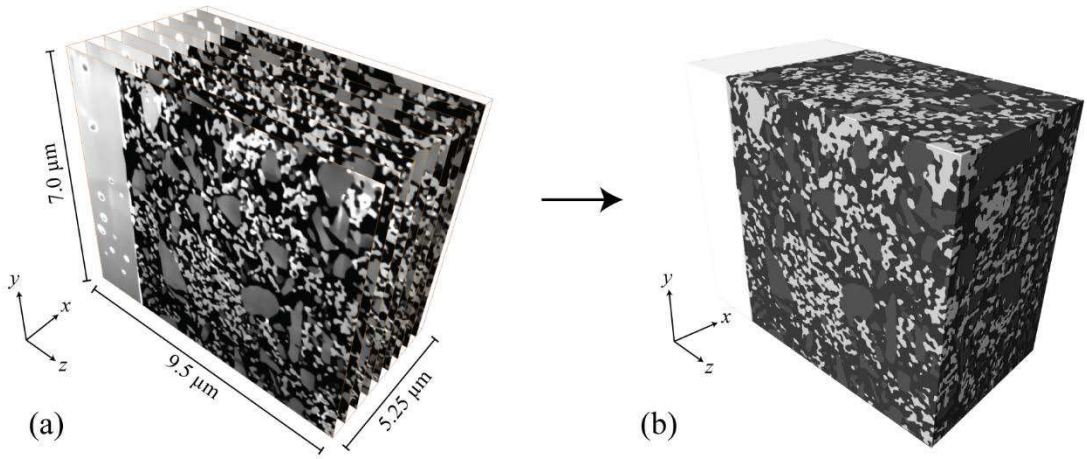

Figure 3. (a) Example of serial images acquired during a slice-and-view run. The bulk YSZ electrolyte is visible to the left of each image, with the composite cathode on the right. (b) Serial images are reconstructed into a representative 3D surface model after segmentation for further quantification. YSZ (white), LSM (gray), and pore (dark gray) phases are shown. Data are from unaged composite cathode sample.

Semi-automated Image Segmentation. A critical component of the reconstruction process is the image segmentation, where each pixel (or voxel, in 3D) is assigned to a particular phase (see Figure 3(b)). Beginning with high-quality images is of utmost importance, and greatly facilitates the segmentation process. A number of different techniques were tested, but ultimately a semi-automated process using Avizo was chosen for its effectiveness, accuracy, and relative ease of use. This process was as follows: an interactive watershed segmentation was first performed to obtain a rough segmentation. This result was typically moderately accurate, but contained a number of errors that needed manual correcting, due to contrast variations within individual particles. A top-hat thresholding step usually corrected errors that occurred within particles and near the particle boundaries. Following this, manual correction of any remaining errors was typically quickly achieved using the "Blow Tool" provided by Avizo. In this manner, a full dataset could be accurately segmented within a few hours, depending on the quality of the initial images.

Three Dimensional Microstructure Reconstruction. Once segmented, 3D reconstructions were created using the Surface Generation modules of Avizo. These models were constructed using constrained smoothing of the segmented labels to limit the overestimation of surface area caused by discrete voxel sizes. The models (example shown in Figure 3(b)) were then used to calculate statistical quantities for each phase, including phase volume, surface area, average particle size, center of gravity, and tortuosity. Average particle size was determined using the BET formula, which estimates spherically-equivalent particle diameter (D) from the phase volume (V) and surface area (S) (10):

$$D = 6 * V/S \quad [1]$$

Tortuosity was calculated by comparing the Euclidean distance between the centroids of each phase on every slice and the projected distance for each dimension (4). Repeating this for the three orthogonal dimensions gave a measure of any anisotropy in the tortuosity. This calculation was implemented in MATLAB.

Finally, the 3D surface model was thinned homotopically in order to develop a 3D model of each phase's connectivity, utilizing the Centerline Tree module of the Avizo

software (11). Using this technique, a variety of parameters can be calculated for each phase, including the number of nodes (*N*) and edges (*E*) in the network, the average topological length (<*L*>), the average connectivity or mean degree (<*k*>), and the maximum observed degree (k_{max}). Definitions of these parameters are given in (2). Use of the Centerline algorithm gives significant improvement compared to the Skeletonization technique that has been used previously (2). The Centerline Tree calculation ensures a calculated network with no loops, and prevents 'starburst' clusters that can appear in the data that artificially inflate <*k*> and k_{max}.

Triple Phase Boundary Analysis. It has been well established that there is a direct relationship between the triple phase boundary length (L_{TPB}) in composite electrodes and the charge transfer and adsorption polarization resistances in the SOFC (3, 12). The L_{TPB} parameter is regarded as one of the most significant microstructural properties in SOFCs, and its calculation provides direct insight into cell performance. Many methods exist to calculate L_{TPB} (13), and this work utilizes an edge connectivity analysis technique documented previously (12). Briefly, TPBs are identified where a voxel edge is shared between all three phases (LSM, YSZ, and pore). The Euclidean distances between each pair of TPB points are added to obtain the total TPB length (L_{TPB}). For comparison, L_{TPB} was also calculated using the volume expansion method. This method computes a volumetric expansion of each phase, giving areas of overlap. Once thinned, the points where all three phases overlap represent the TPB network. This method is implemented in the Avizo software (14).

Results and Discussion

The two samples investigated in this work were sliced, imaged, stacked, and reconstructed using the Avizo software, as described above. The total reconstructed cathode volumes (excluding the bulk electrolyte) for the unaged and H_2O sample were 276.84 μm^3 and 78.77 μm^3, respectively. Due to smaller individual slice sizes of 30 nm, these volumes are smaller than previous works (7), but these slices ensure resolution high enough to sufficiently reconstruct individual particles within the volume. The volume analyzed for the H_2O sample however, is smaller than desired due to an interruption in sample acquisition. This small volume, and in particular, the short *x* dimension (see Figure 4) may preclude the volume from being representative of the sample as a whole. A preliminary analysis of the H_2O sample is provided upon the available data, which will later be corroborated with a larger dataset.

Surface Reconstruction

The 3D surface reconstructions for each sample are shown in Figure 4(a, c). Microstructural details calculated from these surfaces are displayed in Table I.

TABLE I. Surface quantification.

	Material	Surface Area SA (μm^2)	Volume V (μm^3)	SA/V ($\mu m^2/\mu m^3$)	Phase volume fraction (%)	Average particle diameter* (nm)
Unaged	Pore	2633.71	154.84	17.01	55.93%	352.75
	LSM	1137.91	57.66	19.73	20.83%	304.04
	YSZ	1834.36	64.34	28.51	23.24%	210.44
Totals		*5605.98*	*276.84*	*20.25 (avg.)*	*100.00%*	*296.30 (avg.)*
H_2O	Pore	626.68	42.08	14.89	53.42%	402.87
	LSM	357.10	24.85	14.37	31.55%	417.56
	YSZ	381.46	11.84	32.21	15.04%	186.29
Totals		*1365.24*	*78.77*	*17.33 (avg.)*	*100.00%*	*346.20 (avg.)*

* Average particle diameter is calculated using Equation 1.

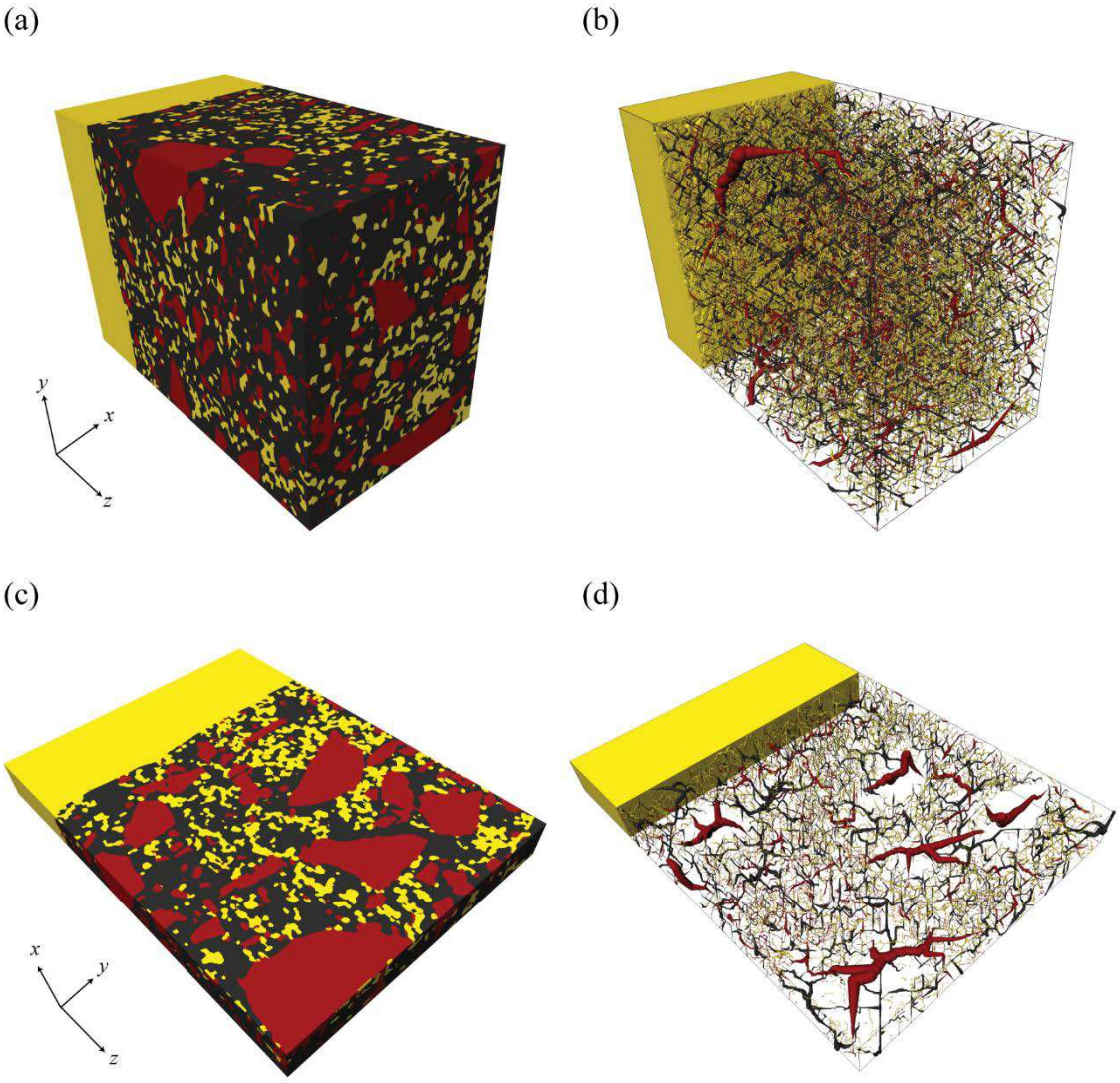

Figure 4. (a) Surface model and (b) skeletonization of unaged reconstructed SOFC composite cathode. Pore space is represented by dark gray, LSM by red (*intermediate gray*), and YSZ by the yellow material (*light gray; color online*). Skeleton thickness is proportional to local phase thickness at each point. ROI dimensions are 5.25 (along *x*) x 7.0 (along *y*) x 9.5 (along *z*) μm^3. (c) Surface model and (d) skeletonization of H_2O SOFC cathode. Colors are same as for unaged sample. ROI dimensions are 1.0 x 8.25 x 11.25 μm^3.

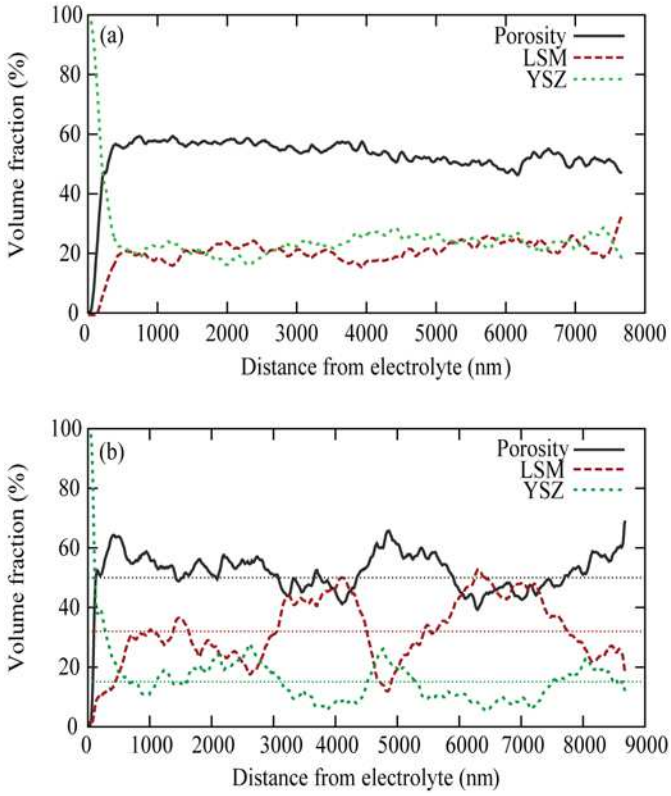

Figure 5. (a) Graded phase fraction along the *z*-axis for unaged sample, as a function of distance from the bulk electrolyte. (b) Same data for H_2O sample, with lines at the mean of each profile to guide the eye. Profiles in (b) have greater variance due to the much smaller *x* dimension sampled, giving rise to non-uniformity, especially at the location of large LSM particles (such as at 3900 and 6800 nm). The unaged sample has similarly sized particles, but (a) shows more uniformity, demonstrating the importance of measuring a sufficiently large and representative sample volume.

The directly comparable quantities are the volume normalized surface area (*SA*/*V*), phase volume fraction, and average particle diameter (*D*, calculated from Equation 1). *SA/V* was calculated using the surface area and volume for each phase independently. In general, the relatively high *SA/V* values measured agree with the fine microstructure observed in the images. The porosity of about 50% for each sample agrees with prior reconstructions of LSM-YSZ composite cathodes (7). Large LSM particles were observed in both samples, the presence of which are due to a large disparity in particle size between the LSM and YSZ present prior to cell processing. This disparity was confirmed by a largely bimodal distribution of particle sizes observed in a dynamic light scattering measurement of the source material.

The phase fractions of LSM (20.83%) and YSZ (23.24%) measured for the unaged sample give a solid phase volume fraction of 47.27/52.73% (LSM/YSZ), in good agreement with the expected ratio of 47.6/52.4%, determined from the cathode source materials' starting weight ratio of 50/50%. This agreement with expected values suggests a valid and representative reconstruction was obtained. Conversely, the solid ratio for the H_2O reconstruction was 67.7/32.3%, in very poor agreement with the source ratio. This implies either a significant change in material properties due to aging or H_2O exposure, or (more likely) that the ROI volume for the H_2O sample may not be representative of the sample as a whole, and thus the results are likely skewed by the presence of large LSM particles (see Figure 4(c) for a visualization of these particles). Further analysis of this sample with a larger ROI volume will be necessary. Additionally, chemical composition analysis will be performed using transmission electron microscopy (TEM) and X-ray energy dispersive spectroscopy (EDS) to investigate whether the formation of secondary phases (such as $La_2Zr_2O_7$ or $SrZrO_3$) may contribute to unexpected variations in the phase volume fractions.

TABLE II. Connectivity quantification.

	Material	N/V (μm^{-3})	E/V (μm^{-3})	$\langle k \rangle$	k_{max}	$\langle L \rangle$ (nm)
Unaged	Pore	32.91	31.96	1.94 ± 1.01	4	328.89
	LSM	23.36	16.92	1.45 ± 0.84	4	259.85
	YSZ	38.32	34.88	1.82 ± 0.99	4	292.37
H_2O	Pore	22.70	22.44	2.34 ± 0.94	4	399.50
	LSM	25.62	17.14	1.34 ± 0.75	4	125.01
	YSZ	38.44	29.92	1.56 ± 0.90	4	257.82

N/V = volume normalized number of vertices (V = total cathode reconstructed volume); E/V = volume normalized number of edge segments; $\langle k \rangle$ = mean degree; k_{max} = maximum degree; $\langle L \rangle$ = average topological length

Phase fractions for each material were evaluated as a function of distance from the composite cathode/electrolyte interface. The results for this analysis are shown in Figure 5. This calculation reveals whether the structure of the cathode changes significantly near the interface with the bulk electrolyte. The relatively flat profiles in Figure 5(a) indicate that little change in the phase fractions occurs over the 8 μm region closest to the bulk electrolyte in the unaged sample. The profiles in Figure 5(b) show much greater variation in the H_2O sample. This is preliminarily attributed to the effect of the large LSM particles observed in this sample, in combination with the very short x dimension analyzed in this data set. The average phase fraction of YSZ is lower than that in the unaged sample, however, and it is unclear whether this is due to the size of the ROI, or an effect of either aging, H_2O exposure, or a combination. This analysis will be repeated on another data collection of the H_2O sample, and compared with an unexposed sample that receives the same thermal treatment to isolate the effects of each process.

Skeletonization and Connectivity

The results of the skeletonization of each phase utilizing the Centerline Tree technique within Avizo are shown in Figure 4(b, d). The corresponding details of the connectivity are reproduced in Table II. As can be seen in these results, using the Centerline algorithm prevents the calculation of 'starburst' clusters that were often observed using the AutoSkeleton technique. These clusters gave rise to artificially high values for the degree of connectivity (k), especially near large particles (see reports of k_{max} in (4) for an example of this). In the present data, the largest degree observed was 4, suggesting a more physically appropriate skeletonization.

A few conclusions can be drawn from the connectivity data in Table II. First, the volume normalized number of nodes and edges are very similar for the LSM and YSZ phases in both samples. This suggests that while the volume observed in the H_2O sample may not be representative of the overall surface characteristics, it may be large enough to capture overall trends in the connectivity. These values are smaller for the pore phase in the H_2O sample though, which together with the larger $\langle k \rangle$, imply a more connected pore structure in this sample. The mean degrees of LSM and YSZ are both higher in the unaged structure, showing a larger connectivity compared to the aged sample. Likewise, these phases have longer $\langle L \rangle$ in the unaged data when compared to the H_2O sample. Further analysis of the H_2O sample is needed to ensure that these effects on connectivity are due to the button cell performance history, rather than the specific ROI volume.

TABLE IV. Tortuosity quantification*.

	Material	τ_x	τ_y	τ_z
Unaged	Pore	1.40	1.30	1.47
	LSM	1.81	1.85	2.60
	YSZ	1.94	1.86	2.07
H_2O	Pore	1.47	1.91	2.41
	LSM	1.97	2.62	3.70
	YSZ	3.20	3.82	4.13

* Tortuosity for each direction (τ_i) is calculated by comparing the center of mass of each phase on the slices orthogonal to direction *i*.

Tortuosity Quantification

The tortuosity is a measure of the difficulty with which a particle can travel through a given volume. In the composite cathode, the tortuosity of the pore structure is particularly relevant to the gas diffusion polarization measured for the cell. Additionaly, the tortuosity of the YSZ phase will affect the path of oxygen ions, although this effect is not expected to be a limiting factor in these LSM/YSZ composite cathodes (7). Tortuosity for each phase was calculated for the two samples, in each of the three orthogonal directions. This was done by reslicing the data after segmentation using Fiji, and running a MATLAB program to calculate the center of mass (centroid) of every phase on each image. A similar module exists in Avizo, but assumes cubic voxels, and will return inaccurate results if this assumption is not met. The script used in this work allows for anisotropic voxel sizes, without affecting the accuracy of the output. The results are displayed in Table III.

As evidenced in Table III, the tortuosity values for the unaged sample appear to be predominantly isotropic. Tortuosity in the *z* direction (τ_z) for the LSM phase is slightly larger, but this could be due to the specific orientation of the larger LSM particles within the volume, and increasing the ROI volume may improve the isotropy of the results. The τ values observed for the unaged pore network are smaller than have been reported for other porous cathodes (3, 5, 15), although each of these cathodes had smaller volume porosities (less than 40%). This indicates easier gas diffusion throughout the structures with higher porosity, as would be expected. The H_2O sample displays greater anisotropy in its tortuosity, with τ_z values substantially larger than the other dimensions for each phase, although the YSZ τ values agree fairly well with those that have been previously reported for LSM/YSZ composite cathodes (7). It is expected that the observed anisotropy in the H_2O sample is due to the high aspect ratio of the volume sampled., These values will be inspected again on a more cubic data set, thus further discussion of the relationship between the H_2O and unaged samples' tortuosities is reserved until that time.

Triple Phase Boundary Quantification

The final microstructural quantification performed in this work was the determination of the total triple phase boundary lengths. As explained previously, this was calculated in two ways. The first involved manually identifying each point that was bordered by all three phases, and calculating the summed length of voxel edges in both the *z*-direction and *x/y*-directions (12). This method may overestimate the total length (see Figure 4 of (14) for an illustration), but provides a relatively simple means by which to calculate L_{TPB}. The second method used to calculate L_{TPB} was the volume expansion method. The results of this method are reported in Table IV. These values are total L_{TPB} lengths, and do not take into

account the fraction of TPB sites that will inevitably be inactive because they are disconnected from a percolated network of each phase. Thus, these values are an upper limit to the density of electrochemically active sties. To directly compare the two samples, the total TPB length (L_{TPB}) was divided by the volume of the reconstructed cathode ($V_{cathode}$) to obtain the volumetric TPB density (ρ_{TPB}). The ρ_{TPB} values found for both samples are similar, but slightly higher than previously reported for similar porous (40-50%) reconstructed and theoretical composite cathodes. Those values ranged from 5.2 – 7.35 μm/μm^3 (7, 16). By comparison, the L_{TPB} values found by edge counting were about an order of magnitude smaller (see Table IV), indicating that further refinement of these methods is necessary to ensure accurate L_{TPB} calculations are obtained.

Regardless of the method used, these results show a significant decrease in ρ_{TPB} for the H_2O sample (when compared with the unaged). As with the other results, it is premature to assign this effect to a particular cause. Both the aging process and exposure to contamination could be catalysts for this change, but the limited ROI volume for the H_2O sample could artificially affect the results as well. Further analysis of a larger sample volume is necessary. Refinement and analysis of the L_{TPB} measurement methods is also required to ensure accurate comparisons between samples, and implementation of an improved centroid-based calculation to measure L_{TPB} (that also calculates the active site fraction) is currently in progress (14).

TABLE V. Preliminary triple phase boundary quantifications.

	L_{TPB}^* (μm)	$V_{cathode}$ (μm^3)	ρ_{TPB}^* (μm/μm^3)
Unaged	3564.34	276.84	12.88
H_2O	802.94	78.77	10.19
	$L_{TPB}^\dagger$ (μm)	$V_{cathode}$ (μm^3)	$\rho_{TPB}^\dagger$ (μm/μm^3)
Unaged	871.33	276.84	3.15
H_2O	94.75	78.77	1.20

*Values calculated using the volume expansion method; †Values calculated using edge summation method

Conclusions

Microstructural reconstruction and quantification was performed on two symmetric LSM/YSZ composite cathode button cell SOFCs that underwent differing performance testing procedures, thermal histories, and environmental exposures. Reconstruction was performed using a 3D nanotomography process with FIB/SEM. Improvements in sample preparation and imaging techniques were discussed. Calculation of surface reconstructions and quantifications of phase surface area, volume, phase fraction, and particle size were reported, along with skeletonization and phase connectivity results. Tortuosity and total triple phase boundary length were calculated and their effects briefly discussed. The effects of sample volume on each of the measured parameters was discussed, and directions for future inquiry outlined. More detailed comparisons between the unaged and H_2O-exposed sample are reserved until sample volume size effects are ruled out.

The FIB/SEM nanotomography methods outlined in this work allow for direct observation of microstructural changes in the SOFC. The technique generates a vast amount of data, and the complimentary data processing provides useful information that can be directly correlated with cell performance. Visualization of this data provides enhanced understanding of the degradation processes that occur during operation, and allow quantification of the effects of contamination and the aging process.

Acknowledgments

The authors would like to acknowledge financial support through US Department of Energy, SECA, Contract No. DEFE0009084. JAT was supported in part by the National Science Foundation Graduate Research Fellowship under Grant No. DGE 1322106. This research was performed in part at the NIST Center for Nanoscale Science and Technology and the authors acknowledge help from John Hagedorn, Wesley Griffin, and Judith Terrill (Scientific Applications and Visualization Group), as well as Joshua Schumacher (CNST) at NIST. JAT would also like to acknowledge the assistance of Nick Vito and Danijel Gostovic in designing and optimizing FIB/SEM experiments and data analysis, and Naoki Shikazono (Univ. Tokyo) and Hiroshi Iwai (Kyoto Univ.) for discussions regarding the volume expansion method.

References

1. C. Sun, R. Hui and J. Roller, *J. Solid State Electrochem.*, **14**(7), 1125 (2009).
2. D. Gostovic, N. J. Vito, K. A. O'Hara, K. S. Jones and E. D. Wachsman, *J. Am. Ceram. Soc.*, **94**(2), 620 (2011).
3. J. R. Smith, A. Chen, D. Gostovic, D. Hickey, D. P. Kundinger, K. L. Duncan, R. T. DeHoff, K. S. Jones and E. D. Wachsman, *Solid State Ionics*, **180**(1), 90 (2009).
4. D. Gostovic, K. A. O'Hara, N. J. Vito, E. D. Wachsman and K. S. Jones, *ECS Trans.*, **16**(51), 83 (2009).
5. D. Gostovic, J. R. Smith, D. P. Kundinger, K. S. Jones and E. D. Wachsman, *Electrochem. Solid-State Lett.*, **10**(12), B214 (2007).
6. L. Holzer and B. Münch, *Microsc. Microanal.*, **15**(2), 130 (2009).
7. J. R. Wilson, A. T. Duong, M. Gameiro, H.-Y. Chen, K. Thornton, D. R. Mumm and S. A. Barnett, *Electrochem. Commun.*, **11**(5), 1052 (2009).
8. A. Buades, B. Coll and J.-M. Morel, in *2005 IEEE Comput. Soc. Conf. Comput. Vis. Pattern Recognit.*, Vol. 2, p. 60. IEEE.
9. J. Schindelin, I. Arganda-Carreras, E. Frise, V. Kaynig, M. Longair, T. Pietzsch, S. Preibisch, C. Rueden, S. Saalfeld, B. Schmid, J.-Y. Tinevez, D. J. White, V. Hartenstein, K. Eliceiri, P. Tomancak and A. Cardona, *Nat. Methods*, **9**(7), 676 (2012).
10. L. Holzer, F. Indutnyi, P. H. Gasser, B. Münch and M. Wegmann, *J. Microsc.*, **216**(Pt 1), 84 (2004).
11. M. Sato, I. Bitter, M. A. Bender, A. E. Kaufman and M. Nakajima, in *Proc. Eighth Pacific Conf. Comput. Graph. Appl.*, p. 281. IEEE Comput. Soc, (2000).
12. K. T. Lee, N. J. Vito and E. D. Wachsman, *J. Power Sources*, **228**, 220 (2013).
13. H. Iwai, N. Shikazono, T. Matsui, H. Teshima, M. Kishimoto, R. Kishida, D. Hayashi, K. Matsuzaki, D. Kanno, M. Saito, H. Muroyama, K. Eguchi, N. Kasagi and H. Yoshida, *J. Power Sources*, **195**(4), 955 (2010).
14. N. Shikazono, D. Kanno, K. Matsuzaki, H. Teshima, S. Sumino and N. Kasagi, *J. Electrochem. Soc.*, **157**(5), B665 (2010).
15. F. Zhao, T. J. Armstrong and A. V. Virkar, *J. Electrochem. Soc.*, **150**(3), A249 (2003).
16. B. Kenney, M. Valdmanis, C. Baker, J. G. Pharoah and K. Karan, *J. Power Sources*, **189**(2), 1051 (2009).